Remote Sensing of Environment 158 (2015) 56–68

Contents lists available at ScienceDirect

Remote Sensing of Environment

journal homepage: www.elsevier.com/locate/rse

Extracting High Temperature Event radiance from satellite images and correcting for saturation using Independent Component Analysis

Talfan Barnie *, Clive Oppenheimer

Department of Geography, University of Cambridge, Downing Place, Cambridge CB2 3EN, UK

ARTICLE INFO

Article history:
Received 9 August 2014
Received in revised form 23 October 2014
Accepted 25 October 2014
Available online 1 December 2014

Keywords:
SEVIRI
Independent Component Analysis
Thermal anomaly
High Temperature Event

ABSTRACT

We present a novel method for extracting the radiance from High Temperature Events (HTEs) recorded by geostationary imagers using Independent Component Analysis (ICA). We use ICA to decompose the image cube collected by the instrument into a sum of the outer products of independent, maximally non-Gaussian time series and images of their spatial distribution, and then reassemble the image cube using only sources that appear to be HTEs. Integrating spatially gives the time series of total HTE radiance emission. In this study we test the technique on a number of simulated HTE events, and then apply it to a number of volcanic HTEs observed by the SEVIRI instrument. We find that the technique performs well on small localised eruptions and can be used to correct for saturation. The technique offers the advantage of obviating the need for a priori knowledge of the area being imaged, beyond some basic assumptions about the nature of the processes affecting radiance in the scene, namely that (i) HTE sources are statistically independent from other processes, (ii) the radiance registered at the sensor is a linear mixture of the HTE signal and those from other processes, and (iii) HTE sources can be reliably identified for the reconstruction process. This results in only five free parameters — the dimensions of the image cube, an estimate of the data dimensionality and a threshold for distinguishing between HTE and nonHTE sources. While we have focused here on volcanic HTEs, the methodology can, in principle, be extended to studies of other kinds of HTEs such as those associated with biomass burning.

1. Introduction

Satellite images have been used to observe thermal emissions from High Temperature Events (HTEs) for over four decades, including terrestrial volcanic activity (e.g. Gawarecki, Lyon, & Nordberg, 1965; Glaze, Francis, & Rothery, 1989; Hanel et al., 1979; Harris et al., 1997; Oppenheimer, 1991), wildfires (e.g. Justice et al., 2002; Kaufman et al., 1998; Roberts & Wooster, 2008), burning fossil fuels (Casadio, Arino, & Minchella, 2012; Kwarteng & Bader, 1993) and eruptions on the Jovian moon Io (e.g. Carr, 1986; Davies, 1996; McEwen et al., 1998). Frequently the total radiance emitted (spatially integrated, in band radiance with units of W m^{-2} μm^{-1} sr^{-1}) by the HTE as a function of time is of interest and is used to derive some useful physical parameter such as radiative power, fire fuel consumption or lava effusion rate (e.g. Harris et al., 2000; Roberts, Wooster, & Perry, 2004; Roberts et al., 2005). However, isolating the HTE radiance from other sources, such as reflected sunlight and thermal emission from ground, clouds and atmosphere as well as instrument response effects such as stray light image artefacts and saturation is difficult. For single images, a relationship between neighbouring pixels is frequently used, for example mean neighbour subtraction or the band ratio method, however these methods are prone to large errors (Wooster & Kaneko, 2001). Alternatively, the non-HTE processes can be explicitly modelled, for instance including background surface temperature as a free parameter in subpixel thermal unmixing (although this is usually assumed a priori, e.g. Oppenheimer, 1993). However such approaches require additional assumptions or independent sources of information. If sequences of images are available, time series based techniques can be applied, for instance Kalman filters have been used to identify anomalous radiance values (Van Den Bergh & Frost, 2005; Van Den Bergh, Udahemuka, & Van Wyk, 2009; Zakšek, Shirzaei, & Hort, 2013). Geostationary imagers are particularly suited to the time series approach due to their consistent acquisition geometry, which excludes complicating factors such as changes in view angle, pixel size and irregular acquisition intervals which make analysing data from Low Earth Orbit (LEO) imagers more difficult.

Given this regular sampling in space, time and wavelength by geostationary sensors, the sensor can be thought of as generating a consistently sampled hypercube of data. Mining this hypercube for signals of interest can be considered a 'big data' problem (e.g. Sellars et al., 2013), which lends itself to matrix factorization (Skillicorn, 2012). The image cube is 'flattened' and represented as a matrix, which is decomposed into a number of

* Corresponding author at: Laboratoire Magmas et Volcans, 5 rue Kessler, 63038 Clermont Ferrand Cedex, France.
E-mail addresses: T.Barnie@opgc.univ-bpclermont.fr (T. Barnie), co200@cam.ac.uk (C. Oppenheimer).

http://dx.doi.org/10.1016/j.rse.2014.10.023

matrices that reveal some fundamental structure of the data. In this study, we use Independent Component Analysis (ICA) (Stone, 2004) to decompose the data matrix into a matrix of statistically independent sources and a mixing matrix that determines the contribution of each source to each signal in the data matrix, in an attempt to separate the HTE sources from other sources of radiance. ICA has been used extensively in remote sensing, e.g. for de-noising satellite gravity data from the GRACE instrument and estimating continental hydrology (Frappart, Ramillien, Maisongrande, & Bonnet, 2010; Frappart et al., 2011), cloud masking Meteosat images (Macías-Macías, García-Orellana, González-Velasco, & Gallardo-Caballero, 2003), unmixing hyperspectral data (Nascimento & Bioucas Dias, 2005; Tu, 2000), analysing the spatial distribution of crop types from MODIS images (Ozdogan, 2010), change detection between images (Zhong & Wang, 2006) and processing SAR images (Fiori, 2003) amongst other applications. In this study we extend the application of ICA to the extraction of HTE radiance time series.

The advantage of the ICA approach is that it makes no assumptions about the nature of the physical processes contributing to the radiance registered at the sensor beyond mutual statistical independence and a linear mixing model. No ancillary information such as surface type, numerical weather prediction data, and model of the local diurnal cycle, is required to extract the HTE radiance registered at the sensor. In some circumstances, ICA can also be used to correct for instrument saturation.

In this study, we apply ICA to time series of images from the geostationary SEVIRI imager, and test the procedure on a number of simulated and observed volcanic eruptions. In the next section we describe the SEVIRI instrument, the source of the data used in the real world case studies. In Section 3 we present an overview of ICA and our application of it to the retrieval of HTE radiance and correcting for saturation. In Section 4 we present the results for the simulations and each case study and in Section 5 we assess the effectiveness of the technique.

2. Datasets

In this section we present an overview of the geostationary imager used to test the technique. We chose the SEVIRI imager as it is currently the most advanced geostationary multispectral imager with a field of view that includes numerous active volcanoes, and selected two volcanic events with spatial and temporal characteristics that lend themselves to the application of ICA (spatially localised, effectively a point source on the scale of a SEVIRI pixel, some saturation, little to no plume and cloud cover) to test the algorithm as a proof of concept.

The SEVIRI instrument is a multispectral imager aboard the Meteosat 2nd generation geostationary meteorological satellites operated by EUMETSAT. The instruments provide coverage of Africa, Europe and the Middle East at intervals of 15 min or less in 12 channels across the visible, short wave and thermal infrared. The sampling interval at nadir is 1 km for the panchromatic and 3 km for the other bands, with an overlap factor (detector size to sampling distance) of 1.6 (Pasternak, Hollier, & Jouan, 1993). The pixel spacing and IFOV size increase radially from the subsatellite point as the view angle increases (Müller, 2010). The SEVIRI instrument operates on a whisk-broom principal, sweeping the Instantaneous Field Of View (IFOV) of each detector across the surface of the Earth in an east–west direction while the satellite spins at 100 rpm, and while an adjustable mirror steps successive scan lines South to North (Aminou, 2002; Aminou, Jacquet, & Pasternak, 1997). In this study we use level 1.5 data in which the instrument counts are radiometrically calibrated and resampled onto a regular grid (Just, 2000), and convert the radiance to units of W m^{-2} μm^{-1} sr^{-1}. The viewing geometry is stable temporally and spectrally, with a relative error in the alignment between two consecutive images of 0.3 km at the SubSatellite Point (SSP) or 0.1 of a pixel and a misregistration between bands is 0.1 km in the E–W and N–S directions. As a result of this stable view geometry and band alignment, each pixel in a time series of images can be considered a time series of radiances at 12 different wavelengths measured over a (roughly) constant region of the Earth's surface, a property we leverage in applying Blind Signal Separation in the next section. Most of the SEVIRI bands do not saturate for the range of thermal radiation typical of volcanic eruptions at the pixel integrated scale of a SEVIRI pixel. However, band 4 does saturate for comparatively small events. Radiances significantly in excess of saturation generate saturation artefacts down scan, resulting in an 'after image' radiance anomaly that decays with successive observations. The SEVIRI instrument is currently used for monitoring wildfire and volcanic activity (e.g. Calle, Casanova, & Romo, 2006; Ganci et al., 2012; Gouhier et al., 2012; Hirn, Di Bartola, & Ferrucci, 2009; Roberts et al., 2004).

The majority of recently active volcanoes lie at the margins of the Earth disc visible from the METEOSAT geostationary orbits, in Iceland, Reunion and Italy, resulting in oblique view angles and large pixel areas. Nyamuragira and Nyiragongo in the Democratic Republic of Congo lie closer to nadir, however these volcanoes are frequently obscured by cloud. Recent activity in the Afar Depression in northern Ethiopia is comparatively close to nadir and has occurred in a relatively cloud free arid environment, and thus provides the optimal test cases and are the focus of this paper — we choose the May 2010 Manda Hararo fissure eruption and the 2010 Erta Ale lava lake overflows as our case studies.

In this study we apply the extraction technique to radiance data from band 4 in units of W m^{-2} μm^{-1} sr^{-1}, and we use the term 'radiance' to refer to this in band radiance, 'spatially integrated radiance' to refer to the radiance summed over all pixels, and 'total radiance' to refer to the radiance summed over all pixels and across time. Statistical extraction techniques are likely to be most useful for band 4 as modelling the background requires a model of both variation in surface temperature and reflected sunlight during the diurnal cycle, and so is the interval of the spectrum where the modelling approach would be most challenging. It is also the band where saturation is the greatest problem, presenting an opportunity to test the saturation correction procedure.

3. Method

An overview of the procedure is given in Fig. 1. Fig. 1A shows the image cube, which can be represented as a sequence of images in time (top) or a collection of time series of radiance, one for each pixel (below). Using ICA, the pixel time series are unmixed into a collection of mutually independent source time series, where each source implicitly defines an image of the magnitude of its contribution to each pixel. We thus decompose the original image cube into a sum of the outer product of each source time series — image pair, as shown in Fig. 1B. We then identify the sources which contain HTE signals, and recompose the image cube restricting the summation to the outer products of HTE sources only. We thus derive an image cube containing only HTE signals, as shown in Fig. 1C. Integrating over each image gives us a time series of the spatially integrated radiant output of all HTE sources. In the next sections, we describe the ICA algorithm used in detail, discuss how HTE sources can be identified and how it can be used to correct for saturation.

3.1. Independent Component Analysis

We treat the time series of radiances associated with each pixel as a vector, which we will refer to as signals, and assume each signal is a linear function of a number of processes that contribute radiance to each pixel, which we refer to as sources. The relationship between the signals and sources can be expressed as a matrix equation known as the generative equation:

$$X = A \cdot S \tag{1}$$

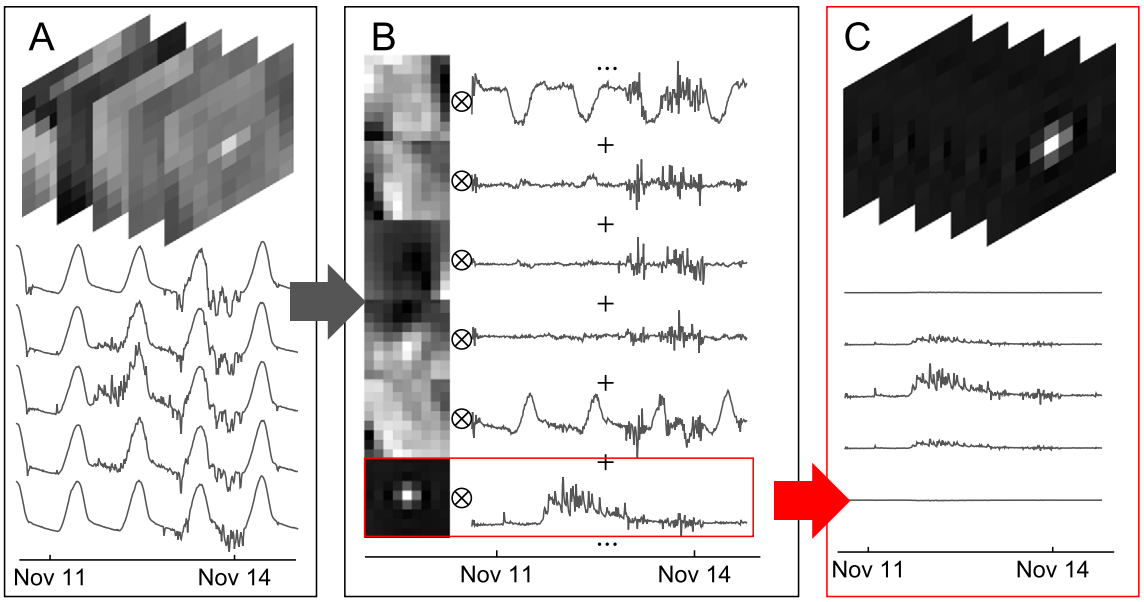

Fig. 1. Summary of the volcanic radiance extraction process using the Erta 'Ale 2010 overflows as an example. (A) The image cube can be considered a sequence of images in time or a collection of time series for each pixel — we apply ICA to the pixel time series. A subset of 5 pixels covering an interval of 4 days is shown, offset vertically for clarity. Note the diurnal cycle, positive volcanic thermal anomalies late on the 11th and negative cloud thermal anomalies on the 13th. (B) The data expressed as a sum of the outer products of independent sources isolated by ICA and their spatial distributions — a subset of 6 sources for the period between the 11th and the 15th are shown. The images on the left show the spatial distribution of selected sources plotted in the graphs on the right; black indicates a low contribution to that pixel, white a high contribution. The sole volcanic source is highlighted in red. (C) The sum of the outer product of the volcanic sources and their spatial distribution (in this case, for just one source) give the volcanic radiance time series for each pixel.

where X is the matrix of signals, with each row the radiance time series for a single pixel, S is the matrix of sources, where each row is the radiance time series for a single source, and A is the mixing matrix, where each row defines a mixing vector. A mixing vector is a list of coefficients that determine the magnitude of the contribution of each source to a given signal, so the first row of A determines the relative mixture of sources in the first signal, the second row the mix in the second signal, and so on. The assumption of a linear mixing model is an appealing aspect of ICA as many volcanic eruptions are small on the scale of a SEVIRI footprint, and so can be modelled as point sources contributing linearly to neighbouring pixels weighted by the point spread function — this property will be leveraged to apply a correction for saturation effects later.

The process of extracting matrices A and S from X is a matrix decomposition, and is underdetermined, requiring extra assumptions to obtain a unique solution (Skillicorn, 2012), for example, if one assumes that the sources are uncorrelated, or nonnegative, or sparse, one obtains the statistical analysis techniques of principal component analysis, nonnegative matrix factorization and sparse component analysis respectively. These techniques are frequently referred to as Blind Signal Separation, as the source signals and mixing system are unknown, and only basic assumptions about them (e.g. sparsity and linearity) are made (Comon & Jutten, 2010). For ICA, the extra assumption we make that permits a unique decomposition is that each source is a series of instances of a random variable with a non-Gaussian probability distribution such that the sources are statistically independent of each other. The assumption of nonGaussianity is an application of the heuristic that "nonGaussianity is interesting" (Hyvärinen, Karhunen, & Oja, 2001), and is a consequence of the central limit theorem, by which a distribution that is the sum of a number of non-Gaussian distributions tends to become more Gaussian-like. This implies that the more non-Gaussian a source is, the less likely it is to be a mixture of different processes. We therefore apply ICA in the hope that volcanic thermal sources are strongly non-Gaussian and will tend to give more Gaussian signals when mixed with radiative signals from other environmental processes (the diurnal cycle, cloud cover, etc.). Given volcanic thermal signals tend to be isolated discrete events between long periods of quiescence, one might expect the signals to be strongly non-Gaussian a priori.

In this study we use the FastICA algorithm of Hyvärinen (1999) and Hyvärinen et al. (2001), that finds the unmixing matrix, W, an estimate of the inverse of A, by maximising the non-Gaussianity (and statistical independence) of the extracted sources using a fixed point algorithm. The FastICA algorithm consists of an initial prewhitening stage and an iteration stage. In the prewhitening stage the data are centred by subtracting the mean of each signal and then 'rotated' in the data space such that the signals are uncorrelated and any signals that appear to be mostly noise are discarded. This is accomplished by pre-multiplying the centred data by a whitening matrix P, which gives the first k Principal Components (PCs) of the data. Ideally, the number of principal components to be retained would be determined by the data dimensionality, but this can be hard to determine in natural datasets, so a trial and error approach is used — too few PCs retained results in useful information being discarded but too many can result in sources that are isolated spikes due to overfitting (Hyvärinen, Särelä, & Vigário, 1999). The iteration stage then finds an orthogonal rotation matrix that further rotates the signals in data space such that they are oriented in directions that are nonGaussianity maxima. Each unmixing vector, which is a row of W, thus defines a projection of the whitened data along a direction that is a nonGaussian maximum — these are the sources. The relationship between the sources and the signals is given by

$$S = W \cdot P \cdot X_C \tag{2}$$

where X_C is the matrix of centred signals, P is the whitening matrix, W is the unmixing matrix and S is the source matrix. The size of the contribution of the sources to each pixel is given by

$$Y = P^{+} \cdot W^{-1} \tag{3}$$

where P^{+} is the pseudo inverse of the whitening matrix P, W^{-1} is the inverse of the unmixing matrix W, and Y is the matrix of the spatial maps of the contributions of each source to each signal. Each source

can thus be considered a time series vector in the time dimension or an image vector in the space dimension. For more details, see Appendix A.

The centred signals are therefore the dot product of the source matrix S and the spatial contribution matrix Y:

$$X_C = Y \cdot S \tag{4}$$

However Eq. (4) can also be expressed as a sum of outer products, which is given by

$$X_C = \sum_i y_i \otimes s_i \tag{5}$$

where s_i is the vector for the ith source given by the ith row of S, y_i is the spatial contribution for the ith source given by the ith column of Y, and $\otimes$ denotes the outer product. The advantage of this representation is that the outer product $y_i \otimes s_i$ represents that particular source as an image cube, giving the amount of radiance that source contributes to each pixel at each point in time, and Eq. (5) describes the original data as the sum over all the source image cubes. If the HTE sources can be identified, then the summation can be limited to the HTE image cubes, giving an image cube containing the total HTE radiance in each pixel at each point in time.

The ICA model still holds if the original data are linearly filtered by multiplication by a matrix from the right (Hyvärinen & Oja, 2000), such that the algorithm can be applied to the filtered data, but the sources are found using the original unfiltered data. This is a useful property as filtering the data can improve source separation, for instance by increasing source smoothness that increases independence and by reducing noise (Pignat et al., 2013). In this study it was occasionally necessary to filter the raw radiance data by differencing the time series over an interval of 96 observations to suppress the diurnal cycle.

3.2. Combining the sources

The signals are recombined by (i) identifying the sources that have isolated HTE radiance, (ii) subtracting the nonzero background from the source and its spatial contribution (taken as the mean of the edge pixels around the spatial contribution image, and the mean of the first few hundred source values), and (iii) taking the outer product of the zeroed source and spatial contribution to get the radiance contribution to each pixel. In cases where the HTE is effectively a point source on the scale of a SEVIRI pixel there is usually only one and it can be found by inspection. However it may be more effective to automatically classify HTE sources where large numbers of sources would have to be laboriously inspected, for instance when conducting numerous tests using randomly generated simulated HTEs, or where the HTE is spatially complex, such as a large advancing lava flow or scattered and migrating wildfires where there may be numerous HTE sources. In this study we automatically classify the sources as HTE/not HTE by means of a 'HTE index', calculated by taking the product of the magnitude of the skewness of the image and time series vectors. HTE sources tend to be very localised in space and time giving a high skewness for the time series and image, and we take the magnitude since sources are only specified up to sign, and so can give a positive or negative skew value. In this study, we identify the HTE source by choosing the one with the highest HTE index as all of our modelled and observed HTEs are effectively point sources on the scale of the SEVIRI pixel and are accounted for by a single source, however a threshold could be used where more than one HTE source is expected.

This approach effectively has five free parameters, the width and height in pixels and the length in images of the image cube to process, an estimate of the dimensionality of the data (how many PCs to retain), and in more complicated cases some HTE index threshold for distinguishing between HTE and nonHTE sources.

3.3. Saturation correction

Extracting the sources using Independent Component Analysis permits for saturation correction. In this approach, we treat the saturated pixels as missing data (for this study, we assume that the down scan 'after image' effect mentioned earlier is negligible). Due to the large size of the instrument Point Spread Function (PSF), any given point source emitting radiance will be sampled by a number of pixels, weighted by the magnitude of the PSF of each pixel above that point. If the radiance is intense enough to saturate a given pixel, a neighbouring pixel with a lower sensitivity at that geographic location may record the full time series unsaturated. We illustrate this with an example from the May 2010 Manda Hararo fissure eruption in Fig. 2. The HTE source is a fissure and advancing lava flow that is small on the scale of a SEVIRI pixel, however given the large size of the PSF, the signal is registered in many neighbouring pixels. Despite the fact that the pixel directly above the eruption saturates during peak volcanic activity, neighbouring pixels faithfully record the variation in radiance over the whole eruption, albeit at reduced amplitude and therefore lower signal to noise ratio.

We therefore simply exclude the signal from the pixel(s) that contain saturated observations, and rely on neighbouring pixels to faithfully record the HTE signal. Fig. 3 shows the effect of progressively removing pixels on the extracted HTE source, again using the May 2010 Manda Hararo eruption as an example. Removing just the saturated pixel results in a 'steeper' source (red curve in Fig. 3A) as the artificially low saturation values are removed from consideration. As further pixels are removed, the extracted source becomes noisier, however it is still recognisable even after all pixels in a 3×3 window surrounding the saturated pixel have been removed. Plotting the HTE source for all pixels against that for unsaturated pixels (Fig. 3C) shows an excellent correlation (R^2 of 0.998) for images where the central pixel is unsaturated, showing that with or without the saturated pixel, for unsaturated observations, ICA is extracting the same radiance pattern, validating our assumption that the same source is being recorded in all pixels in the neighbourhood of the eruption. The relationship breaks down for images where the central pixel is saturated, as expected.

The HTE source extracted from unsaturated pixels is then used to calculate the contribution of that source to each pixel, including saturated pixels, according to equation

$$Y = X \cdot \check{S}^{+} \tag{6}$$

where X and $\check{S}$ are the submatrices of the data and source matrices with times that contain one or more saturated observations (columns) removed (for a derivation, see Appendix A). The image cube giving the HTE signal in each pixel is given by the outer product of source and spatial contribution pair, as before.

In summary, to perform the saturation correction, we apply ICA on the pixel time series with the time series with saturated pixels excluded to get the source, find the spatial contribution image for that source by excluding images with saturated pixels, and then reconstruct the image cube as before.

3.4. Simulated volcanic eruptions

It is difficult to assess the effectiveness of the technique as measurements of remote, hazardous volcanic events at the scale of a SEVIRI pixel are nearly impossible to ground truth. However we can test the procedure on a synthetic dataset. We use synthetic datasets chosen to resemble the actual examples presented in this study to check the validity of those results as a proof of concept; we do not attempt to exhaustively check the procedure's effectiveness on a wide range of different types of HTE, nor the effects of varying algorithm parameters.

We produce a 'synthetic volcanic eruption' radiance curve described by a plausible functional form (and hopefully therefore a plausible

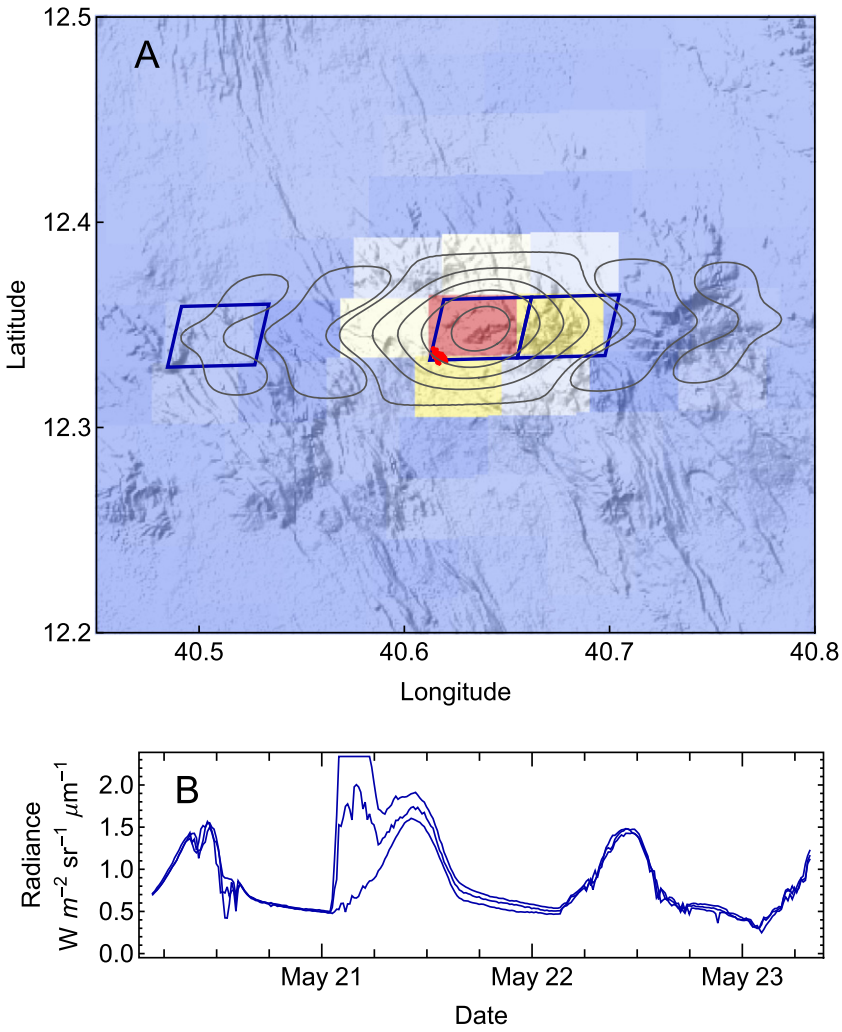

Fig. 2. The signal from an effective point source is registered in many pixels. (A) SEVIRI band 4 (3.9 μm) image of the May 2010 Manda Hararo eruption acquired 2010/05/21 at 03:12 UTC, overlaid on topography from the SRTM digital elevation model. Blue colour indicates low radiance, red high radiance. Contours show the point spread function for the central pixel, red polygon extent of erupted lava. PSF calculated using the method of Lee and Atkinson (2000) from the instrument MTF (Aminou et al., 1999). The registration between the image and the lava flow location has an error on the order of a few hundred metres. Note that although the lava flow is small on the scale of a single pixel, the large spatial extent of the PSF results in the volcanic radiance contributing substantially to pixels in a 7 × 7 pixel window. The saturation correction technique works on the principle that if the HTE signal is sufficient to saturate pixels with high PSF values over the radiance source, neighbouring pixels with a lower sensitivity over the source will record the source unsaturated. (B) Radiance time series from pixels outlined in blue in (A). The time series for the pixel over the lava flow saturates during the peak of the eruption, whereas that for the neighbouring pixel faithfully records the full variation in radiance. Even three pixels away from the lava flow, a very weak HTE signal is apparent.

statistical distribution of values, which is what the ICA algorithm acts upon) by convolving an area effusion rate function with a cooling function to model the radiance emitted due to the progressive emplacement of infinitesimal area elements of cooling material in a manner similar to that of Carr (1986) and Davies (1996). For the area effusion rate function we use a linear waxing and exponential waning function similar to the trend for volumetric effusion rate curves noted by Wadge (1981), and for the cooling curve we use an exponential, analogous to cooling curves observed of basalt surfaces (Ball, Pinkerton, & Harris, 2008). This gives a radiance curve defined by 6 parameters, start time, stop time, time of maximum effusion rate, effusion rate decay coefficient, cooling rate decay coefficient, and a scaling factor that sets the maximum radiance value. We assume that the volcanic source of radiance is a point source on the scale of a SEVIRI pixel, calculate the SEVIRI PSF following the method of Lee and Atkinson (2000) using the instrument MTF (Aminou, Ottenbacher, Jacquet, & Kassighian, 1999), and weight the contribution of the signal to each pixel by the PSF. This signal is then added to a HTE free radiance time series in an image cube covering the southern segment of the Manda Hararo rift during May to June 2010. The volcanic radiances are added during a cloud free interval. We model three scenarios; 'simple', 'complex', and 'saturated'. In the 'simple' scenario, we use the single waxing waning function to create a radiance signal analogous to that of a small basaltic fissure eruption like the Manda Hararo event. In the 'complex' scenario, we simulate the Erta 'Ale lava lake overflows by summing a number of waxing and waning functions offset in time to simulate a number of small lava lake overflows, and add the convolution with the cooling curve to a triangle function that simulates the slow rise and fall of the lava lake surface into and out of the instrument field of view. The 'saturated' scenario is the same as the 'simple', except we clip the radiances at 2.337 W m^{-2} sr^{-1} μm^{-1}, the saturation limit for SEVIRI band 4, and use these to test the saturation correction.

4. Results

In this section we present the results of applying the HTE extraction process to the simulated volcanic eruption scenarios, and two case studies. For the simulated volcanic eruptions, we test the

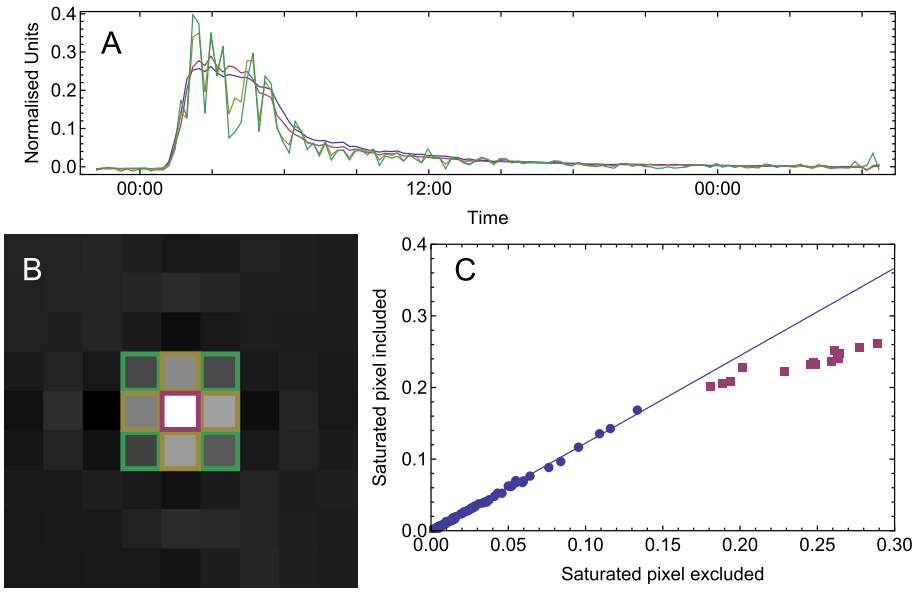

Fig. 3. The effect of progressively excluding pixels from the ICA algorithm on the extracted HTE source. (A) Extracted sources; blue curve: all pixels, red curve: central saturated pixel excluded, yellow curve: saturated pixel and all pixels in 4 cardinal directions excluded, green curve: all pixels in a 9 × 9 window centred on the saturated pixel excluded. Note that as more pixels are excluded, the extracted signal becomes noisier. (B) SEVIRI image acquired at peak of eruption, showing pixels excluded in (A). Pixels are colour coded to curves. (C) Plot of sources extracted from all pixels (blue curve in (A)) against source extracted from all unsaturated pixels (red curve in (A)). Observations where no pixel is saturated in the image plotted in blue, observations where the central pixel is saturated plotted in red. Note that for images where the central pixel is unsaturated, both sources exhibit a linear relationship with an R^2 of 0.998, however for a saturated central pixel they exhibit a poorer correlation and a shallower slope due to underestimation of the radiance due to saturation.

effectiveness of the procedure in two ways: Firstly we find the coefficient of determination (r^2) between the simulated and extracted source and spatial contribution (the PSF function in this case) to see if the 'shape' of these vectors are recovered accurately (we don't check that they have the right magnitude given that ICA only recovers them up to sign and scaling). Secondly, we test the absolute accuracy of the procedure by comparing the volcanic radiance integrated across all pixels and observations to see if we recover the same total radiant output from the event.

For the real HTE events, the original, decomposed and recombined datasets are large, so presenting an overview of all extracted sources and HTE signals for each dataset is difficult. As a result, to give an overview of the decomposition into sources stage, we present a selection of the sources extracted by the FastICA algorithm showing the range of HTE, diurnal cycle and cloud process dominated sources found. For the recombination to give the HTE signal per pixel, we then show examples of the recovered HTE signals for a representative selection of pixels, as well as the original signals, and their residuals after subtracting the HTE signal. Finally, we show the extracted total HTE signal for the given event, showing the total radiant output in that band from the HTE event integrated over all pixels, which is typically the parameter of interest.

4.1. Simulations

For the 'simple' scenario, we simulated 50 random volcanic eruptions (6 free parameters per eruption) and added them to a cloud free period in a 9 × 9 pixel by 1500 image data cube covering the lower part of the Manda Hararo rift. The image cube was prefiltered, and ICA was performed with the first 40 PCs, and the HTE source was assumed to be that with the highest HTE index. Radiance time series for the pixel directly above the source for all 50 simulations are shown in Fig. 4A. The volcanic source and spatial contribution image are recovered with a high degree of accuracy up to offset, sign and scaling as shown in Fig. 4B, where the r^2 for both relationships are above 0.9 for all simulations. The relationship between total simulated and total recovered volcanic radiance was found to be

$$recovered = 0.998 \times simulated - 5.70 \quad (7)$$

with an r^2 of 0.988, as shown in Fig. 4C, close to the expected 1:1 relationship.

For the 'complex' scenario, we simulated 50 random volcanic eruptions, each consisting of 30 simple eruptions summed with a triangle function (124 free parameters for each simulation), added to a cloud free period in a 9 × 9 pixel window × 2500 image data cube. Radiance time series for the pixel directly above the source for a selection of simulations are shown in Fig. 5A. The image cube was prefiltered, and ICA was performed with 40 PCs and the source with the highest HTE index was assumed to be the volcanic signal. The r^2 between the modelled and recovered volcanic sources and spatial contribution was again usually above 0.9 (Fig. 5A), however there was greater scatter, including a recovered source with r^2 near 0 for both where the algorithm failed to identify the volcanic source. The relationship between the total modelled and total recovered volcanic radiance was found to be

$$recovered = 1.07 \times original - 36 \quad (8)$$

with a correlation coefficient r^2 of 0.983.

For the 'saturation' scenario, we modelled 50 random volcanic eruptions using the same procedure as in the 'simple' scenario, and then clipped the radiance values to the saturation value of 2.337 W m^{-2} sr^{-1} μm^{-1} after adding to the background 9 × 9 pixel by 2500 image data cube. Example radiance time series for the central pixel in the 9 × 9 window are shown in Fig. 6A. The image cube was prefiltered, and ICA was performed using 40 PCs and the source with the highest HTE index was assumed to be the volcanic source. In this analysis we grouped the simulations by the number of pixels that became saturated. The r^2 for the sources and spatial contributions for simulations with one saturated pixel are all above 0.9, however as the

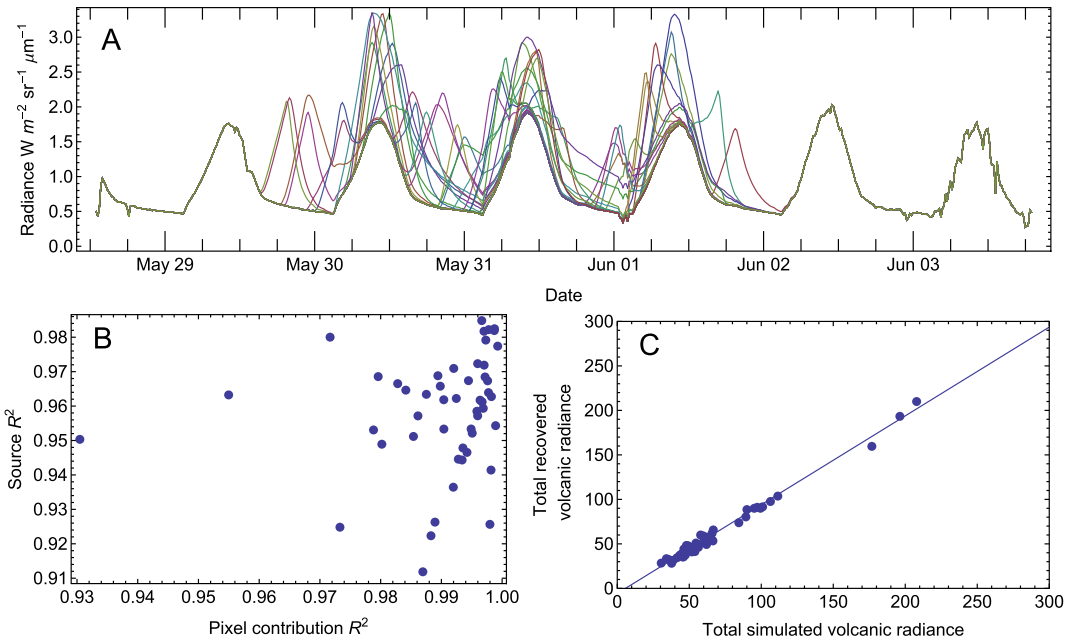

Fig. 4. A) Fifty simulated radiance curves showing the background and added synthetic volcanic signal for the central pixel in the 9 by 9 pixel window. B) Plot of correlation coefficients between the modelled and recovered source (Y axis) and modelled and recovered contributions of the source to each pixel (X axis). C) Plot of total recovered volcanic radiance against total simulated volcanic radiance. Best fit line gives slope of 0.998 indicating that recovered total radiance is consistently underestimated slightly, an intersect of −5.70, and with an R^2 of 0.988.

number of saturated pixels goes up, the correlation coefficients, and the fidelity of the recovered source, decreases (Fig. 6B). This has a large effect on the relationship between modelled and recovered total volcanic radiance (Fig. 6C), where the relationship is given by

$$recovered = 26.0 + 0.876 \times simulated \quad (9)$$

with an r^2 of 0.992 for single saturated pixel simulations. As the number of saturated pixels increases, the recovered total volcanic radiance increasingly underestimates the original. This effect appears to be less pronounced for high values of total radiance, which may be a function of simulations with long durations with a greater proportion of nonzero, nonsaturated values.

4.2. The 2010 Erta 'Ale overflows

The 2010 Erta 'Ale overflows were a series of fluctuations in the height of the lava lake at the summit of the Erta 'Ale basaltic shield

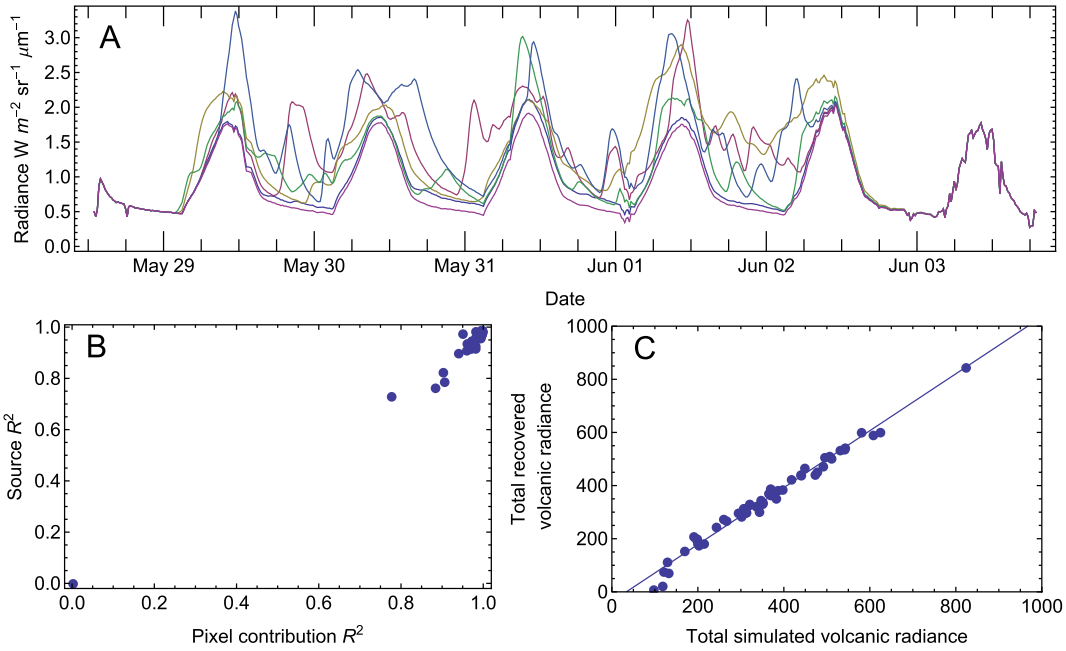

Fig. 5. A) Subset of the fifty simulated radiance curves showing the background and added synthetic volcanic signal for the central pixel in the 9 by 9 pixel window. B) Plot of correlation coefficients between the modelled and recovered source (y-axis) and modelled and recovered contributions of the source to each pixel (x-axis). C) Plot of total recovered volcanic radiance against total simulated volcanic radiance. Best fit line gives slope of 1.07 indicating that recovered total radiance is consistently overestimated slightly, an intersect of −36.0, and with an R^2 of 0.983.

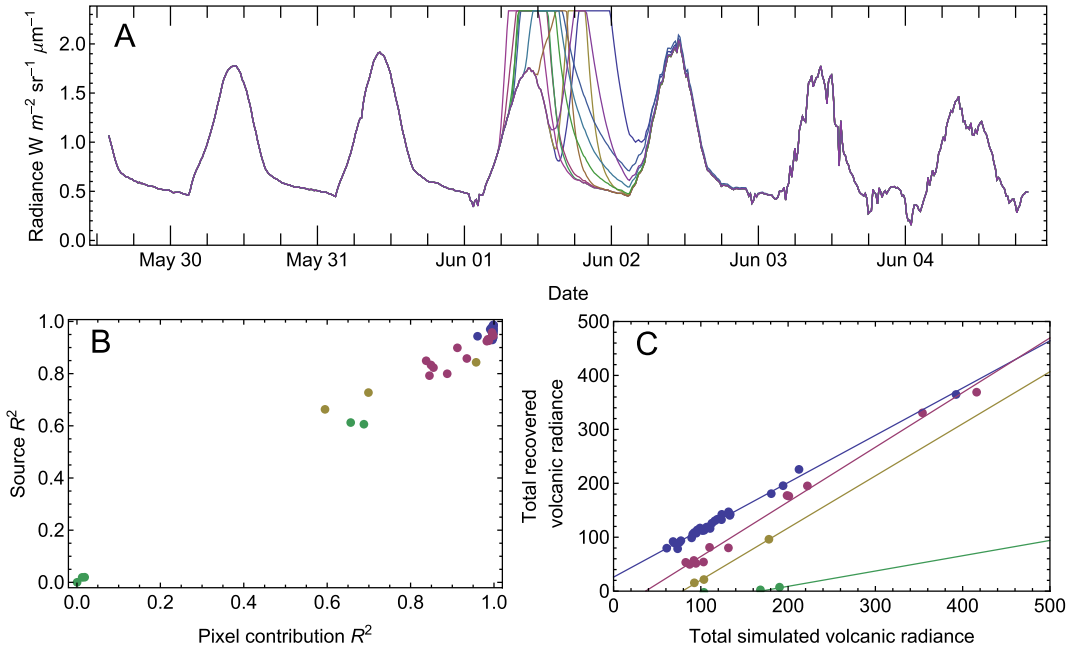

Fig. 6. A) Subset of the fifty simulated radiance curves showing the background and added synthetic volcanic signal for the central pixel in the 9 by 9 pixel window. B) Plot of correlation coefficients between the modelled and recovered source (Y axis) and modelled and recovered contributions of the source to each pixel (X axis). Blue dots are for simulations with a single saturated pixel, red for three, yellow for four and green for five. C) Plot of total recovered volcanic radiance against total simulated volcanic radiance. Best fit line to points with a single saturated pixel gives slope of 0.876 indicating recovered total radiance is consistently slightly underestimated, an intersect of 26.0, and with an R^2 of 0.992.

volcano in the axial volcanic range of the same name in northern Afar (Barberi & Varet, 1970; Field et al., 2012). The lava lake sits in a pit approximately 30 m deep within a 1 km by 3 km caldera at the volcano summit. The increase in height of the lava lake raised the lake surface out of the satellite view shadow below the pit rim and into the field of view of the instrument, resulting in a thermal anomaly. Fluctuations in the lake height varied the proportion of the lake in view, and resulted in overflows onto the caldera floor. Individual overflows were registered as spikes in the SEVIRI radiance time series for the pixel covering the lava lake, and were simultaneously observed by a field team on the ground (Field et al., 2012). Field et al. (2012) isolated the thermal anomaly associated with the lava lake and overflows by subtracting the signal from a neighbouring pixel with no thermal anomaly, however the resulting thermal anomaly signal was still contaminated with a diurnal signal. In this study we attempt to isolate the signal using ICA. We choose this event as it is unusual for a volcanic eruption in being small enough not to saturate band 4. It is also very spatially small and localised, being effectively a point source on the scale of a pixel point spread function, making it a useful test of whether the whisk broom acquisition and resampling significantly undermine the ICA assumption of instantaneous linear mixing. As for the May 2010 Manda Hararo eruption, being in northern Afar, the aridity of the environment, and the relative lack of cloud during this event result in an excellent signal, that has facilitated previous Earth Observations studies (e.g. Oppenheimer & Francis, 1997).

We applied the ICA procedure to time series of radiance from SEVIRI pixels in band 4 in a 9 by 9 window surrounding the lava lake, acquired between 23:57 UTC 2010/10/26 and 01:57 UTC 2010/12/16 using the 40 most significant principal components. Prefiltering was found to be unnecessary in this case. A subset of the sources extracted is shown in Fig. 7. There appeared to be only one volcanic source, which was easily identified by a spatial pattern that resembles the instrument Point Spread Function (consistent with small lava lake footprint compared to the scale of a SEVIRI pixel) and a time series that is flat with positive excursions. Two sources capture the diurnal cycle (sources 2 and 3), and are easily identifiable by their 24 h periodicity and spatial contribution images that reflect variation in surface type across the Erta 'Ale range. The rest are dominated by cloud during periods of cloud cover. Taking the outer product of the volcanic source and its spatial contribution gives the volcanic signal for each pixel in the 9 × 9 window, examples of which are shown in Fig. 8. Subtracting the volcanic signal from the

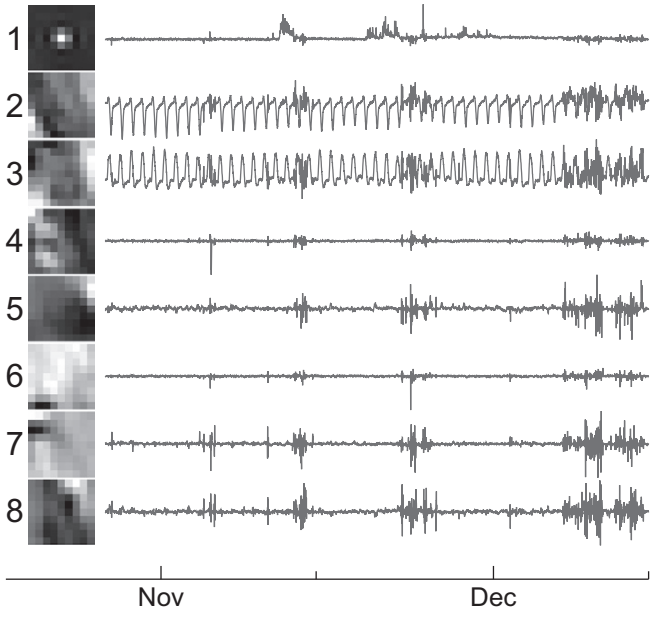

Fig. 7. Selected sources extracted from the SEVIRI image time series of the November 2010 Erta 'Ale overflows using FastICA. The graphs on the right show the temporal variation of each source, the images on the left show the spatial distribution of the source in the 9 by 9 pixel window. Source 1 is the HTE source with a PSF like spatial contribution, sources 2 and 3 describe the diurnal cycle with a 24 hour periodicity and spatial contribution that resembles the landcover distribution surrounding the lava lake. The remaining sources are dominated by cloud noise.

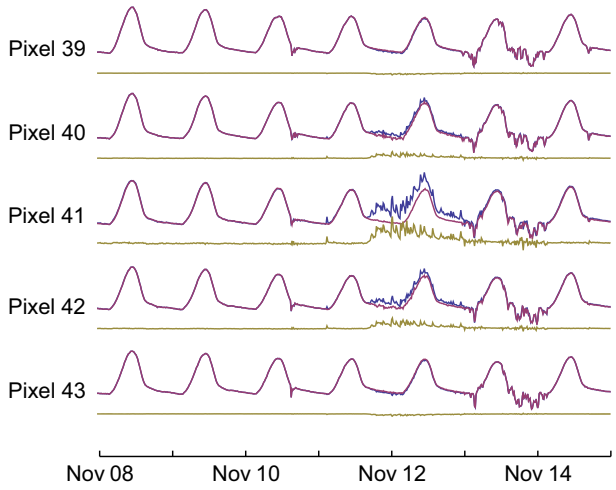

Fig. 8. Comparison of signal (blue curve) extracted volcanic radiance (yellow curve), and the residual after subtracting the volcanic radiance from the signal (red curve) for a subset of the data between 8 and 15 November 2010. Note that the residuals are relatively smooth during periods of HTE radiance, indicating most of the HTE radiance is accounted for by the HTE source.

original signal leaves a residual which should closely resemble the diurnal temperature cycle (in cloud free conditions) — by inspection, this appears to be the case. Summing the volcanic signal in each pixel gives the total volcanic radiant output during the eruption, as shown in Fig. 9. We can get a measure of the noise in the extracted total volcanic radiance by taking the Standard Deviation. During a cloud free period this comes to 0.0239 while during cloudy periods the cloud introduces extra noise, giving a standard deviation of 0.0778. During periods of cloud free volcanic thermal signal, the standard deviation varies between 0.080 and 0.27.

4.3. The May 2010 Manda Hararo Eruption

The May 2010 Manda Hararo eruption was of fissural type and associated with the 14th and last dike intrusion in the Manda Hararo rifting cycle that lasted from 2005 to 2010 in northern Afar, Ethiopia (Ayele et al., 2009; Grandin et al., 2010; Hamling et al., 2009; Wright et al., 2006). During a rifting cycle vertical sheets of magma are intruded along the length of rift segments at plate boundaries, accommodating the divergent motions of the plates by the creation of new crust, a process that has been called 'the quantum event of sea floor spreading' (Delaney et al., 1998). The intrusions take place on a timescale of hours, with tens of dikes intruded over 5 to 10 years, between quiescent periods lasting centuries to millennia. If the intrusions reach the surface, fissural eruptions occur. Most rift segments are underwater at mid ocean ridges making rifting events difficult to observe, so the rare subaerial events such as that at Manda Hararo provide an important glimpse of these 'quantum events'. The aridity and inaccessibility of the Manda Hararo segment make monitoring by remote sensing both applicable and necessary. The May 2010 event intruded 0.081 km^3 of magma in a dike up to 1.6 m wide, 18 km long and up to 9 km deep, and extruded 2.3×10^5 m^3 of lava from a ~600 m long fissure forming a ~2 m thick lava low (Ian Hamling, Barbara Hofmann, personal communication, 2014). The fissure eruption is an ideal test of the ICA method because it is a small, localised event with limited saturation in band 4 and no cloud cover, and is comparatively close to satellite nadir for a volcanic event.

We applied the ICA procedure to a time series of 1500 SEVIRI image subsets in a 9×9 window between 2010/05/16 00:57:00 UTC and 2010/05/31 15:57:00 UTC using the 30 most significant PCs. Again, prefiltering was unnecessary in this example. The central pixel was found to be saturated during the peak of the eruption, so that pixel was excluded from the ICA procedure, as discussed in the saturation correction section. A subset of the extracted sources is shown in Fig. 10. As with the Erta 'Ale overflows, the Manda Hararo eruption was a spatially small event on the scale of a SEVIRI pixel and is partitioned into a single source with a PSF-like spatial distribution, as is the diurnal cycle, and most of the remaining sources are dominated by cloud noise. We find the spatial contribution of the volcanic source using the saturation correction discussed earlier, and take the outer product of the volcanic source and its corrected spatial contribution to obtain an image cube giving the volcanic signal in each pixel. Examples of the original pixel signal, the extracted volcanic signal and the residual are shown in Fig. 11. Again, by inspection, the residual resembles the diurnal cycle without thermal anomalies, with the exception of the period of saturation in pixel 41, where the recovered volcanic signal is greater than that registered due to saturation. Integrating spatially gives the radiance time series shown in Fig. 12. The standard deviation during cloud free periods is 0.0488, during cloudy periods is 0.187, and over the duration of the eruption is 2.24.

5. Discussion

The results from the simulations indicate that for most 'simple' and 'complex' scenarios, the procedure recovers the shape of the source and spatial contribution vectors with a high degree of fidelity, with coefficients of determination typically greater than 0.9. The total radiant output is also recovered with minor systematic bias, and the relationship between the original and recovered values has a high correlation coefficient. For scenarios with a single saturated pixel the total radiance is only slightly underestimated, however as the number of saturated pixels increases the total radiance is increasingly underestimated. From these observations we draw the conclusion that the ICA procedure is valid for the extraction of the thermal signal from HTEs that can be considered point sources at the scale of a SEVIRI pixel, exhibit variations in radiance that are consistent with basic conceptual models of lava flow

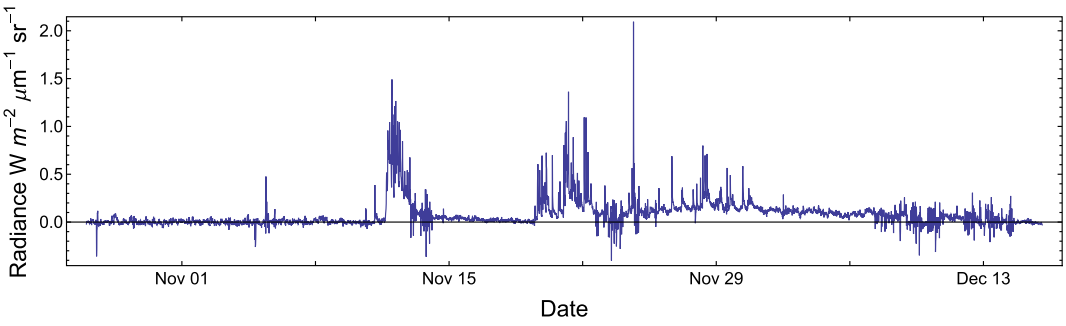

Fig. 9. Spatially integrated volcanic radiance emitted by the November 2010 Erta 'Ale lava lake overflows found by summing the per pixel volcanic radiances. Negative peaks are due to cloud noise.

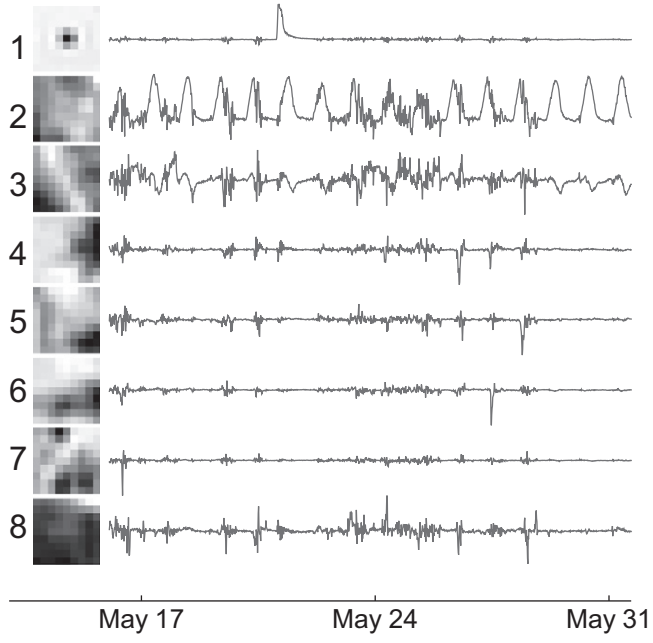

Fig. 10. Selected sources extracted from the SEVIRI image time series of the May 2010 Manda Hararo eruption using FastICA. The graphs on the right show the temporal variation of each source, the images on the left show the spatial distribution of the source in the 9 by 9 pixel window. The central pixel time series was excluded from the ICA procedure due to saturation. Source 1 is the HTE source with a PSF like spatial contribution and a waxing and waning source time series radiance pattern, sources 2 and 3 are dominated by the diurnal cycle with a 24 h periodicity, and the remaining sources are dominated by cloud noise.

emplacement, and have saturation in not more than one or two pixels. However it should be noted that the simulations do not take into account the delays in acquisition time down and across scan as a function of the SEVIRI instrument's whisk-broom mode of operation which violates the assumption of linear mixing of sources in pixels, as the time delay results in the volcanic radiance being sampled at slightly different times in each pixel (0.6 s difference between scan lines), a problem

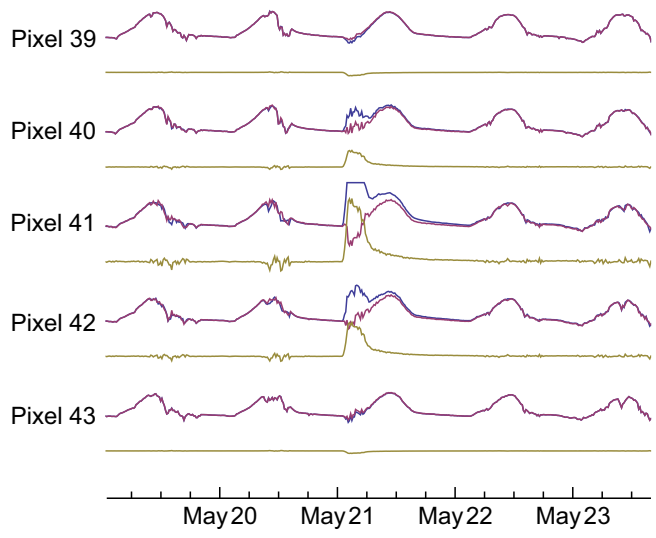

Fig. 11. Comparison of signal (blue curve) extracted volcanic radiance (yellow curve), and the residual after subtracting the volcanic radiance from the signal (red curve) for a subset of the data between 19 and 24 May 2010. Note the residual curves are relatively smooth during the eruption period, indicating the HTE source accounts for most of the volcanic radiance, with the exception of pixel 41 which lies directly above the eruption and experienced saturation.

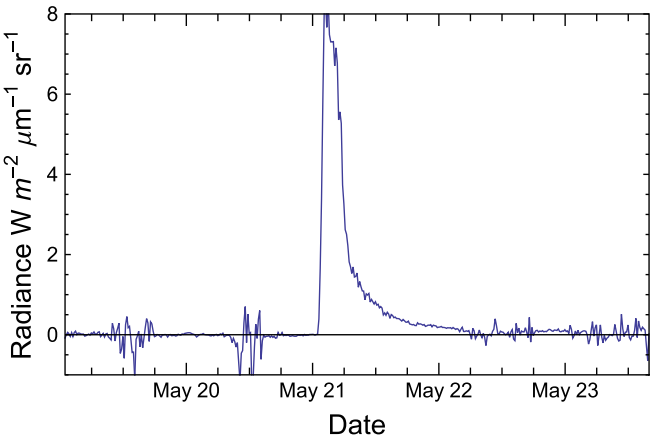

Fig. 12. Spatially integrated volcanic radiance emitted by the May 2010 Manda Hararo eruption found by summing the per pixel volcanic radiances. Negative peaks are due to cloud noise.

documented before in sequentially acquired thermal images of volcanic activity (Oppenheimer, Rothery, Pieri, Abrams, & Carrere, 1993). The simulated volcanic radiance is also added directly to the background, so the effect of varying atmospheric conditions altering the signal on a per pixel basis is not modelled. In addition, the resampling that takes place during the conversion of level 1 to level 1.5 data is not taken into account, however the effect of this, if any, on the assumptions made by the ICA model is not clear. The simulations also do not take into account of the impact of plumes on the recovered HTE, which might be expected to partially or totally obscure the HTE, resulting in an underestimation or gaps in the recovered total radiance. The plume radiance signal may also be strongly correlated with the HTE source, resulting in a recovered source that mixes HTE and some plume radiance. Thus the presence of plume may violate the FastICA assumptions of source linear mixing and independence. However, the former may only affect HTEs substantially obscured by the plume while the latter may be alleviated by the effect of ambient environmental effects on the plume lessening the correlation with HTE radiance. It should also be noted that cloud contamination affects all HTE retrieval techniques, and doubly affects the neighbouring pixel subtraction method, as the effect of cloud contamination is propagated between pixels by subtracting one from the other. The effect of all of these complications would have to be investigated in more detail before the approach could be reliably operationalized. The simulated eruption scenarios can thus be considered to establish the validity of the ICA model under 'ideal' conditions.

Having established that under ideal conditions, volcanic signals analogous to real examples can be extracted accurately, we applied the procedure to the two case studies. ICA successfully decomposed the image cube into sources that represent different physical processes, successfully isolating the volcanic and diurnal signals into separate sources, with appropriate spatial contribution images (PSF-like for the volcanic sources and resembling landcover variation for the diurnal cycle). A close examination of the residuals after subtraction of the recovered per pixel volcanic signal indicates that the recovered volcanic source accounts for most of the radiance of volcanic origin. This appears to confirm the fundamental assumptions that sources of volcanic radiance are sufficiently non-Gaussian in nature to be separated from other sources of radiance by ICA, and that the mixing model is close enough to linear that nonlinearities resulting from whisk broom acquisition and resampling between level 1 and level 1.5 data do not substantially interfere in the process. The noise in the recovered signal varies greatly depending on the amount of cloud present; during clear periods the noise was found to be between 0.0239 and 0.0488 W m^{-2} sr^{-1} μm^{-1}, however during cloudy periods it increased to between 0.0778 and 0.187 W m^{-2} sr^{-1} μm^{-1}. Cloud contamination is likely not modelled well by ICA since an 'ideal', unchanging cloud moving across a number

of pixels would contribute to pixels at different times, despite constituting a single source, violating the linear mixing assumption, and would be better modelled with a convolutive ICA model (e.g. Douglas, Gupta, Sawada, & Makino, 2007), however such models are complex and computationally expensive, and are beyond the scope of this paper. Cloud contamination appears to be accommodated in regular ICA with instantaneous mixing as an increase in 'noise' in all sources when cloud is present. Neither of the case studies exhibited significant plumes that resulted in obscuration of, or correlation with, the HTE.

The HTEs studied appear to be recovered well, as supported by the simulations. However HTEs that vary in radiant output on a timescale comparable to the sampling delay between neighbouring pixels and produce large saturation effects will likely be poorly recovered. The former problem might be alleviated by increasing the number of PCs retained, such that the separate HTE source is recovered for adjacent scans, however the latter will likely remain a problem as the down scan saturation anomaly will contaminate unsaturated pixels directly, and indirectly during resampling, and may be so large as to exclude the PSF of all neighbouring pixels, resulting in a 'sensitivity hole' in which signals are not recorded unsaturated in any pixel.

Finally, in this paper we have modelled our volcanic HTE radiance as a convolution of a cooling curve and an area emplacement curve, based on the ideas of Carr (1986) and Davies (1996). The recovered radiances could be deconvolved with a guessed cooling curve to get an estimate of the area effusion rate provided the assumptions of the simple convolutive model hold, and with multispectral observations, more sophisticated models could be inverted.

6. Conclusions

In this study we have presented an approach for extracting the radiance from High Temperature Events (HTEs) from time series of geostationary satellite images using Independent Component Analysis. We decompose the image cube constructed by the regular sampling in time and space of geostationary imagers into the sum of the outer products of maximally independent nonGaussian radiance sources and their spatial distributions, identify HTE sources on the basis of a HTE index, and sum over the HTE sources to give an image cube with HTE signals only. Integrating over each image then gives the total HTE radiance as a time series. In addition, we take advantage of the fact that a point source is recorded in different pixels at different amplitudes to apply a saturation correction. We have validated this approach for simple, point source, volcanic sources using simulated volcanic radiances based on conceptual models of lava flow emplacement, and applied it to two case studies, the May 2010 fissural eruption of the Manda Hararo rift system and the November 2010 Erta 'Ale lava lake overflows, both of which took place in Afar, Ethiopia. We are able to recover the time series of the spatially integrated volcanic radiant output of both eruptions, and apply a correction for saturation in the case of the May 2010 eruption. Future work could involve further simulations to include multiple point source HTEs and spatially complex HTEs and application of the method to a wider range of HTE phenomena, including wildfires, as well as attempt to improve the saturation correction for larger events.

Acknowledgements

This research was undertaken as part of the NERC consortium project "How does the Earth's crust grow at divergent plate boundaries? A unique opportunity in Afar, Ethiopia" (grant number NE/E005535/1). CO is additionally supported by the UK National Centre for Earth Observation "Dynamic Earth and Geohazards" theme (http://comet.nerc.ac.uk/).

Appendix A

In this appendix we present a more detailed account of the FastICA algorithm of Hyvärinen (Hyvärinen, 1999; Hyvärinen & Oja, 2000; Hyvärinen et al., 2001) as applied to radiance time series, and its application in the case of saturated pixels. Full derivations and more in depth explanations can be found in the aforementioned references, and Stone (2004) gives an excellent introduction to the topic. In the following we use the upper case symbols for matrices, lower case symbols for vectors and functions, the symbol . to denote the dot product between any combination of matrices and vectors and * denotes multiplying each row of a matrix by the corresponding value in a vector.

The FastICA algorithm proceeds in two stages, a prewhitening stage to decorrelate the data, and an iterative stage where a fixed point algorithm is used to find an orthogonal unmixing matrix that gives the maximally independent nonGaussian sources. In the whitening stage the signals are first centred to give each a mean of zero:

$$X_C = X - \overline{X} \tag{A1}$$

where X is the matrix of signals, $\overline{X}$ is a matrix with constant rows equal to the signal means, and X_C is the matrix of centred signals. The centred signals are then decorrelated by finding the premultiplication matrix P that gives the first k principal components, where k is an estimate of data dimensionality (usually chosen by trial and error). The matrix P is found by taking the covariance matrix of the centred sources:

$$C_X = \frac{1}{n} X_C \cdot X_C^T \tag{A2}$$

where n is the length of the signals, X_C^T is the transpose of the centred source matrix and C_X is the covariance matrix. The eigendecomposition is then found

$$C_X = E \cdot \Lambda \cdot E^T \tag{A3}$$

where E and Λ are the eigenvector and eigenvalue matrices respectively, and the matrix P calculated.

$$P = \left(\Lambda^{-1/2} \cdot E\right)_k \tag{A4}$$

where $(\ldots)_k$ denotes retaining the first k row/principal components. The matrix of centred, uncorrelated signals is then given by Z:

$$Z = P \cdot X_C. \tag{A5}$$

Once the signals have been whitened, the fixed point algorithm is applied. Each iteration proceeds in four steps. First, the current estimate of the source matrix $\hat{S}$ is updated from the current estimate of the unmixing matrix W (for the first iteration W is initialised as a random matrix and orthogonalised by Eq. (A9))

$$\hat{S} \leftarrow W \cdot Z. \tag{A6}$$

The current estimate of W is then updated in the direction of increasing nonGaussianity

$$W \leftarrow \frac{1}{N}\left(Z \cdot g\left(\hat{S}\right) - W * \sum\nolimits_{rows} g\prime\left(\hat{S}\right)\right) \tag{A7}$$

where N is the number of observations in a signal, and the function g is a nonlinearity function, which is used to estimate the non—Gaussianity of the source — we use the standard $g(\hat{S}) = Tanh(\hat{S})$, and $g\prime$ denotes its derivative. The step in Eq. (A7) does not enforce the orthogonality condition on, so the matrix is then orthogonalised

$$W \leftarrow \left(W \cdot W^T\right)^{-0.5} \cdot W. \tag{A8}$$

At the end of each iteration i, the current estimate of the unmixing matrix, W_i, is compared with the previous one, W_{i-1}. If the Frobenius norm of the difference of the absolute matrices drops

below a value ε (we take 10^{-5}) as shown in Eq. (A9), the algorithm is stopped, and otherwise steps A6 to A8 are repeated.

$$\|Abs(W_{i-1}) - Abs(W_i)\|_F \leq \varepsilon \tag{A9}$$

where $\|\ldots_F\|$ denotes taking the Frobenius norm of the enclosed matrix. We take the absolute values of the elements of the unmixing matrices before differencing them because ICA only recovers source up to sign — the value of W can be converged, yet the sign of the unmixing vectors (rows) of the matrix can change from one iteration to the next. We implemented the FastICA algorithm in Mathematica, based on the code of Langlois, Chartier, and Gosselin (2010), but with modifications for symmetric orthogonalisation and matrix operations to increase speed.

The contributions of each source to each pixel is then given by

$$Y = P^{+} \cdot W^{-1} \tag{A10}$$

where Y is the spatial contribution matrix, of columns that give the size of the contribution of a given source to each pixel, P^{+} is the pseudoinverse of P and W^{-1} is the inverse of W. Alternatively, Y can be found from Eq. (A11):

$$Y = X_C \cdot S^{+} \tag{A11}$$

where S^{+} is the pseudoinverse of the recovered sources, S. This is useful in the case where signals with one or more saturated observations have been excluded for finding the sources. In this case matrices P and W which give the sources in terms of the reduced number of signals cannot be used to estimate Y; instead we wish to estimate Y from the centred signals with any saturated values removed. We demonstrate how this can be achieved as follows. We start by expressing the unsaturated (but unknown) radiance time series X_C as a function of the known sources S of unknown spatial contributions Y.

$$X_C = Y \cdot S. \tag{A12}$$

We then multiply by an identity matrix with rows removed that correspond to sections of the time series when one or more pixels is saturated, I_S,

$$X_C \cdot I_S = Y \cdot S \cdot I_S. \tag{A13}$$

This gives us an equation for Y in terms of

$$Y = (X_C \cdot I_S) \cdot (S \cdot I_S)^{+} \tag{A14}$$

or

$$Y = X_C \cdot \check{S}^{+} \tag{A15}$$

which gives us the spatial contribution matrix Y as a function of the known, unsaturated radiances $\check{S}$ and the unsaturated signals X_C. The saturation correction is thus dependent upon the matrix $(X_C \cdot I_S) \cdot (S \cdot I_S)^{+}$ being a good approximation to $X_C \cdot S^{+}$.

References

Aminou, D. M. A. (2002). MSG's SEVIRI instrument. *ESA Bulletin-European Space Agency* (pp. 15–17).

Aminou, D. M. A., Jacquet, B., & Pasternak, F. (1997). Characteristics of the Meteosat second generation (MSG) radiometer/imager: SEVIRI. *Sensors, Systems, and Next-Generation Satellites, 3221*, 19–31.

Aminou, D. M. A., Ottenbacher, A., Jacquet, B., & Kassighian, A. (1999). Meteosat second generation: On-ground calibration, characterisation and sensitivity analysis of SEVIRI imaging radiometer. *Earth Observing Systems Iv, 3750*, 419–430.

Ayele, A., Keir, D., Ebinger, C., Wright, T. J., Stuart, G. W., Buck, W. R., et al. (2009). September 2005 mega-dike emplacement in the Manda-Harraro nascent oceanic rift (Afar depression). *Geophysical Research Letters, 36*, L20306 ((5 pp.)-L20306 (5 pp.)).

Ball, M., Pinkerton, H., & Harris, A. J. L. (2008). Surface cooling, advection and the development of different surface textures on active lavas on Kilauea, Hawai'i. *Journal of Volcanology and Geothermal Research, 173*, 148–156.

Barberi, F., & Varet, J. (1970). The Erta Ale volcanic range (Danakil depression, northern afar, Ethiopia). *Bulletin of Volcanology, 34*, 848.

Calle, A., Casanova, J. L., & Romo, A. (2006). Fire detection and monitoring using MSG spinning enhanced visible and infrared imager (SEVIRI) data. *Journal of Geophysical Research — Biogeosciences, 111*, http://dx.doi.org/10.1029/2005JG000116.

Carr, M. H. (1986). Silicate volcanism on Io. *Journal of Geophysical Research-Solid Earth and Planets, 91*, 3521–3532.

Casadio, S., Arino, O., & Minchella, A. (2012). Use of ATSR and SAR measurements for the monitoring and characterisation of night-time gas flaring from off-shore platforms: The North Sea test case. *Remote Sensing of Environment, 123*, 175–186.

Comon, P., & Jutten, C. (2010). *Handbook of blind source separation*. Elsevier.

Davies, A. G. (1996). Io's volcanism: Thermo-physical models of silicate lava compared with observations of thermal emission. *Icarus, 124*, 45–61.

Delaney, J. R., Kelley, D. S., Lilley, M. D., Butterfield, D. A., Baross, J. A., Wilcock, W. S. D., et al. (1998). The quantum event of oceanic crustal accretion: Impacts of diking at mid-ocean ridges. *Science, 281*, 222–230.

Douglas, S. C., Gupta, M., Sawada, H., & Makino, S. (2007). Spatio-temporal FastICA algorithms for the blind separation of convolutive mixtures. *IEEE Transactions on Audio, Speech and Language Processing, 15*, 1511–1520.

Field, L., Barnie, T., Blundy, J., Brooker, R. A., Keir, D., Lewi, E., et al. (2012). Integrated field, satellite and petrological observations of the November 2010 eruption of Erta Ale. *Bulletin of Volcanology, 74*, 2251–2271.

Fiori, S. (2003). Overview of independent component analysis technique with an application to synthetic aperture radar (SAR) imagery processing. *Neural Networks, 16*, 453–467.

Frappart, F., Ramillien, G., Leblanc, M., Tweed, S. O., Bonnet, M. -P., & Maisongrande, P. (2011). An independent component analysis filtering approach for estimating continental hydrology in the GRACE gravity data. *Remote Sensing of Environment, 115*, 187–204.

Frappart, F., Ramillien, G., Maisongrande, P., & Bonnet, M. P. (2010). Denoising satellite gravity signals by independent component analysis. *IEEE Geoscience and Remote Sensing Letters, 7*, 421–425.

Ganci, G., Harris, A. J. L., Del Negro, C., Guehenneux, Y., Cappello, A., Labazuy, P., et al. (2012). A year of lava fountaining at Etna: Volumes from SEVIRI. *Geophysical Research Letters, 39*, http://dx.doi.org/10.1029/2012GL051026.

Gawarecki, S. J., Lyon, R. J. P., & Nordberg, W. (1965). Infrared spectral returns and imagery of the Earth from space and their application to geological problems. *Scientific Experiments for Manned Orbital Flight, Science and Technology Series, 4*, 13–133.

Glaze, L., Francis, P. W., & Rothery, D. A. (1989). Measuring thermal budgets of active volcanos by satellite remote-sensing. *Nature, 338*, 144–146.

Gouhier, M., Harris, A., Calvari, S., Labazuy, P., Guéhenneux, Y., Donnadieu, F., et al. (2012). Lava discharge during Etna's January 2011 fire fountain tracked using MSG-SEVIRI. *Bulletin of Volcanology, 74*, 787–793.

Grandin, R., Socquet, A., Jacques, E., Mazzoni, N., De Chabalier, J. B., & King, G. C. P. (2010). Sequence of rifting in Afar, Manda-Hararo rift, Ethiopia, 2005–2009: Time-space evolution and interactions between dikes from interferometric synthetic aperture radar and static stress change modeling. *Journal of Geophysical Research — Solid Earth, 115*.

Hamling, I. J., Ayele, A., Bennati, L., Calais, E., Ebinger, C. J., Keir, D., et al. (2009). Geodetic observations of the ongoing Dabbahu rifting episode: New dyke intrusions in 2006 and 2007. *Geophysical Journal International, 178*, 989–1003.

Hanel, R., Conrath, B., Flasar, M., Kunde, V., Lowman, P., Maguire, W., et al. (1979). Infrared observations of the Jovian system from Voyager 1. *Science, 204*, 972–976.

Harris, A. J. L., Butterworth, A. L., Carlton, R. W., Downey, I., Miller, P., Navarro, P., et al. (1997). Low-cost volcano surveillance from space: Case studies from Etna, Krafla, Cerro Negro, Fogo, Lascar and Erebus. *Bulletin of Volcanology, 59*, 49–64.

Harris, A. J. L., Murray, J. B., Aries, S. E., Davies, M. A., Flynn, L. P., Wooster, M. J., et al. (2000). Effusion rate trends at Etna and Krafla and their implications for eruptive mechanisms. *Journal of Volcanology and Geothermal Research, 102*, 237–270.

Hirn, B., Di Bartola, C., & Ferrucci, F. (2009). Combined use of SEVIRI and MODIS for detecting, measuring, and monitoring active lava flows at erupting volcanoes. *IEEE Transactions on Geoscience and Remote Sensing, 47*, 2923–2930.

Hyvärinen, A. (1999). Fast and robust fixed-point algorithms for independent component analysis. *IEEE Transactions on Neural Networks, 10*, 626–634.

Hyvärinen, A., Karhunen, J., & Oja, E. (2001). *Independent Component Analysis*. Wiley-Blackwell.

Hyvärinen, A., & Oja, E. (2000). Independent component analysis: Algorithms and applications. *Neural Networks, 13*, 411–430.

Hyvärinen, A., Särelä, J., & Vigário, R. (1999). Bumps and spikes: Artefacts generated by independent component analysis with insufficient sample size. *Workshop on Independent Component Analysis and Blind Signal Separation (ICA'99)* (pp. 425–429).

Just, D. (2000). *Seviri level 1.5 data. First Msg Rao Workshop, 452*. (pp. 29–37), 29–37 (228).

Justice, C. O., Giglio, L., Korontzi, S., Owens, J., Morisette, J. T., Roy, D., et al. (2002). The MODIS fire products. *Remote Sensing of Environment, 83*, 244–262.

Kaufman, Y. J., Justice, C. O., Flynn, L. P., Kendall, J. D., Prins, E. M., Giglio, L., et al. (1998). Potential global fire monitoring from EOS-MODIS. *Journal of Geophysical Research, [Atmospheres], 103*, 32215–32238.

Kwarteng, A. Y., & Bader, T. A. (1993). Using satellite data to monitor the 1991 Kuwait oil fires. *Arabian Journal for Science and Engineering, 18*, 95–115.

Langlois, D., Chartier, S., & Gosselin, D. (2010). An introduction to Independent Component Analysis: InfoMax and FastICA algorithms. *Tutorial in Quantitative Methods for Psychology, 6*, 31–38.

Lee, A. C. L., & Atkinson, N. C. (2000). *The impact of aliasing on MSG images: Final report*. UK Meteorological Office.

Macías-Macías, M., García-Orellana, C., González-Velasco, H., & Gallardo-Caballero, R. (2003). Independent Component Analysis for cloud screening of Meteosat images. In J. Mira, & J. Álvarez (Eds.), *Artificial neural nets problem solving methods*. Berlin Heidelberg: Springer.

McEwen, A. S., Keszthelyi, L., Spencer, J. R., Schubert, G., Matson, D. L., Lopes-Gautier, R., et al. (1998). High-temperature silicate volcanism on Jupiter's moon Io. *Science*, *281*, 87–90.

Müller, J. (2010). *MSG level 1.5 image data format description. EUM/MSG/ICD/105.*

Nascimento, J. M. P., & Bioucas Dias, J. M. (2005). Does independent component analysis play a role in unmixing hyperspectral data? *IEEE Transactions on Geoscience and Remote Sensing*, *43*, 175–187.

Oppenheimer, C. (1991). Lava flow cooling estimated from Landsat thematic mapper infrared data: The Lonquimay Eruption (Chile, 1989). *Journal of Geophysical Research*, *96*, 21865–21878.

Oppenheimer, C. (1993). Thermal distributions of hot volcanic surfaces constrained using three infrared bands of remote sensing data. *Geophysical Research Letters*, *20*, 431–434.

Oppenheimer, C., & Francis, P. (1997). Remote sensing of heat, lava and fumarole emissions from Erta'Ale volcano, Ethiopia. *International Journal of Remote Sensing*, *18*, 1661–1692.

Oppenheimer, C., Rothery, D. A., Pieri, D. C., Abrams, M. J., & Carrere, V. (1993). Analysis of airborne visible/infrared imaging spectrometer (AVTRIS) data of volcanic hot spots. *International Journal of Remote Sensing*, *14*, 2919–2934.

Ozdogan, M. (2010). The spatial distribution of crop types from MODIS data: Temporal unmixing using Independent Component Analysis. *Remote Sensing of Environment*, *114*, 1190–1204.

Pasternak, F., Hollier, P., & Jouan, J. (1993). *Seviri, the new imager for Meteosat 2nd-generation. Igarss'93: Better understanding of earth environment*, *Vols I–IV*. (pp. 1094–1099), 1094–1099 (2160).

Pignat, J. M., Koval, O., Van De Ville, D., Voloshynovskiy, S., Michel, C., & Pun, T. (2013). The impact of denoising on independent component analysis of functional magnetic resonance imaging data. *Journal of Neuroscience Methods*, *213*, 105–122.

Roberts, G. J., & Wooster, M. J. (2008). Fire detection and fire characterization over Africa using Meteosat SEVIRI. *IEEE Transactions on Geoscience and Remote Sensing*, *46*, 1200–1218.

Roberts, G., Wooster, M. J., & Perry, G. W. (2004). *High temporal resolution fire radiative energy and biomass combustion estimates derived from MSG Seviri. Proceedings of the Second MSG RAO Workshop*, *582*. (pp. 57–63), 57–63 (172).

Roberts, G., Wooster, M. J., Perry, G. L. W., Drake, N., Rebelo, L. -M., & Dipotso, F. (2005). Retrieval of biomass combustion rates and totals from fire radiative power observations: Application to southern Africa using geostationary SEVIRI imagery. *Journal of Geophysical Research*, *110*, http://dx.doi.org/10.1029/2005JD006018 D21111.

Sellars, S., Nguyen, P., Chu, W., Gao, X., Hsu, K. -L., & Sorooshian, S. (2013). Computational earth science: Big data transformed into insight. *Eos, Transactions American Geophysical Union*, *94*, 277–278.

Skillicorn, D. (2012). *Understanding complex datasets: Data mining with matrix decompositions Chapman & Hall/CRC.*

Stone, J. V. (2004). *Independent Component Analysis.* MIT Press.

Tu, T. -M. (2000). Unsupervised signature extraction and separation in hyperspectral images: A noise-adjusted fast independent component analysis approach. *Optical Engineering*, *39*, 897–906.

Van Den Bergh, F., & Frost, P. E. (2005). A multi-temporal approach to fire detection using MSG data. *Multitemp05, Biloxi, Mississipi* (pp. 150–160).

Van Den Bergh, F., Udahemuka, G., & Van Wyk, B. J. (2009). Potential fire detection based on Kalman-driven change detection. *2009 IEEE International Geoscience and Remote Sensing Symposium (IGARSS 2009), 12–17 July 2009 Cape Town, South Africa. IEEE, IV-77-IV-IV-80.*

Wadge, G. (1981). The variation of magma discharge during basaltic eruptions. *Journal of Volcanology and Geothermal Research*, *11*, 139–168.

Wooster, M. J., & Kaneko, T. (2001). Testing the accuracy of solar-reflected radiation corrections applied during satellite shortwave infrared thermal analysis of active volcanoes. *Journal of Geophysical Research*, *106*, 13381–13393.

Wright, T. J., Ebinger, C., Biggs, J., Ayele, A., Yirgu, G., Keir, D., et al. (2006). Magma-maintained rift segmentation at continental rupture in the 2005 Afar dyking episode. *Nature*, *442*, 291–294.

Zakšek, K., Shirzaei, M., & Hort, M. (2013). Constraining the uncertainties of volcano thermal anomaly monitoring using a Kalman filter technique. *Geological Society, London, Special Publications*, *380*, 137–160.

Zhong, J., & Wang, R. (2006). Multi-temporal remote sensing change detection based on independent component analysis. *International Journal of Remote Sensing*, *27*, 2055–2061.